

**Science**

 AAAS

**Electrically Induced Optical Emission from a Carbon Nanotube FET**

J. A. Misewich, *et al.*

*Science* **300**, 783 (2003);

DOI: 10.1126/science.1081294

***The following resources related to this article are available online at [www.sciencemag.org](http://www.sciencemag.org) (this information is current as of January 3, 2008 ):***

**Updated information and services**, including high-resolution figures, can be found in the online version of this article at:

<http://www.sciencemag.org/cgi/content/full/300/5620/783>

This article **cites 20 articles**, 7 of which can be accessed for free:

<http://www.sciencemag.org/cgi/content/full/300/5620/783#otherarticles>

This article has been **cited by** 273 article(s) on the ISI Web of Science.

This article has been **cited by** 5 articles hosted by HighWire Press; see:

<http://www.sciencemag.org/cgi/content/full/300/5620/783#otherarticles>

This article appears in the following **subject collections**:

Chemistry

<http://www.sciencemag.org/cgi/collection/chemistry>

Information about obtaining **reprints** of this article or about obtaining **permission to reproduce this article** in whole or in part can be found at:

<http://www.sciencemag.org/about/permissions.dtl>

7. A. Müller *et al.*, *Angew. Chem. Int. Ed. Engl.* **41**, 3604 (2002).
8. J. Bai, E. Leiner, M. Scheer, *Angew. Chem. Int. Ed.* **41**, 783 (2002).
9. J. Bai, A. V. Virovets, M. Scheer, *Angew. Chem. Int. Ed.* **41**, 17370 (2002).
10. Because of a large content of  $\text{CH}_2\text{Cl}_2$  molecules in the crystal lattice, the crystals obtained by layering these solutions with *n*-pentane are in general weakly diffracting. Starting from a 1:2 reaction mixture between  $[\text{Cp}^*\text{Fe}(\eta^5\text{-P}_5)]$  (**3**) and  $\text{CuCl}$ , we obtained moderately diffracting crystals of an orthorhombic space group with  $a = 55.12(1)$  Å,  $b = 45.034(9)$  Å,  $c = 25.755(5)$  Å, and  $V = 63936$  Å<sup>3</sup>, which contained exclusively neutral molecules of **1**. Thus, the ionic product **2** seems to be formed only by a reaction with a deficiency of  $\text{CuCl}$  (ratio Fe:Cu in **1** is about 1:2). The crystals obtained in the 1:1 reaction can be formulated as  $\text{1}_3\text{2}$ , which describes the existence of three molecules of **1** and one molecule of **2** in the unit cell.
11. Experimental and crystallographic details are available as supporting material on Science Online.
12. Such unusual molecule/ion pair disordering is nonetheless in good agreement with the diffraction data. Efforts to describe this molecule in a completely molecular manner lead to poor-quality values of the refinement (e.g., an  $R_1$  value of 0.1371 versus 0.1257 for the disordered ionic model), resulting in a large residual difference electron peak and a large atomic displacement parameter for the ball-connected atom  $\text{Cu55}$  [see (11) for details].
13. There is no difference in the solubility and in the NMR spectroscopic properties of these solutions between  $\text{1}_3\text{2}$  (10) and **1**.
14. Mean deviation from the plane of the central *cyclo*- $\text{P}_5$  ring is 0.0054 Å and of the peripheral *cyclo*- $\text{P}_5$  rings 0.0021 Å.
15. R. Blom, T. Brück, O. J. Scherer, *Acta Chem. Scand.* **43**, 458 (1989).
16. O. J. Scherer, T. Brück, G. Wolmershäuser, *Chem. Ber.* **121**, 935 (1988).
17. O. J. Scherer, T. Brück, *Angew. Chem. Int. Ed. Engl.* **26**, 59 (1987).
18. A. Hirsch, B. Nuber, *Acc. Chem. Res.* **32**, 795 (1999), and literature cited herein.
19. C. Möschel, M. Jansen, *Z. Anorg. Allg. Chem.* **625**, 175 (1999).
20. I. Silaghi-Dumitrescu, F. Lara-Ochoa, P. Bishof, I. Haiduc, *J. Mol. Struct. (Theochem.)* **367**, 47 (1996).
21. I. Silaghi-Dumitrescu, F. Lara-Ochoa, I. Haiduc, *J. Mol. Struct. (Theochem.)* **370**, 17 (1996).
22. V. Tozzini, F. Buda, A. Fasolino, *J. Phys. Chem. B* **105**, 12477 (2001).
23. Dedicated to Professor Otto J. Scherer on the occasion of his 70th birthday. This work was comprehensively supported by the Deutsche Forschungsgemeinschaft and the Fonds der Chemischen Industrie. We thank D. Fenske (Karlsruhe, Germany) for measurement of the x-ray data set and H. Eckert (Münster, Germany) for the <sup>31</sup>P MAS-NMR investigations. We also thank the Siberian Supercomputing Center for the use of the MVS-1000M computer for the structural refinement.

**Supporting Online Material**  
[www.sciencemag.org/cgi/content/full/300/5620/781/DC1](http://www.sciencemag.org/cgi/content/full/300/5620/781/DC1)  
 Materials and Methods  
 Fig. S1  
 Tables S1 to S5  
 References

3 December 2002; accepted 20 March 2003

## Electrically Induced Optical Emission from a Carbon Nanotube FET

J. A. Misewich,\* R. Martel, Ph. Avouris, J. C. Tsang, S. Heinze, J. Tersoff

Polarized infrared optical emission was observed from a carbon nanotube ambipolar field-effect transistor (FET). An effective forward-biased p-n junction, without chemical dopants, was created in the nanotube by appropriately biasing the nanotube device. Electrical measurements show that the observed optical emission originates from radiative recombination of electrons and holes that are simultaneously injected into the undoped nanotube. These observations are consistent with a nanotube FET model in which thin Schottky barriers form at the source and drain contacts. This arrangement is a novel optical recombination radiation source in which the electrons and holes are injected into a nearly field-free region. Such a source may form the basis for ultrasmall integrated photonic devices.

Nanowires and nanotubes are being investigated for use in nanoscale optoelectronic and photonic applications because of their capability for efficient transport of carriers. Recently, great progress was achieved in the synthesis of direct band-gap material nanowires and nanowire superlattices (1–3), and their electroluminescence properties may allow novel light sources to be fabricated.

In the fabrication of light-emitting devices from nanowires made of conventional semiconductor materials, two major approaches have been taken. In one approach, independent p-doped and n-doped nanowires are assembled into a crossed structure to form a p-n

junction (2). Alternatively, a nanowire superlattice is grown by modulation of the reactant supply during nanowire growth (3). Both approaches require great precision in the fabrication steps.

We have focused instead on semiconductor single-walled carbon nanotubes (s-SWNTs), which have proven to be well suited for making field effect transistors (FETs) (4–6). Despite the approximately 1.4-nm diameter of the nanotube, this channel can switch as much as 6  $\mu\text{A}$ , corresponding to a current density  $>10^8$  A/cm<sup>2</sup>. More recently, both p-type and n-type nanotube FETs have been fabricated, and logic gates have been demonstrated (7–9). The ability of nanotubes to support p-type as well as n-type behavior, in combination with the direct band gap of these materials, suggests the possibility of a nanoscale optical source using carbon nanotubes. Although the Raman spectra of carbon nanotubes have received extensive attention

(10, 11), little work has been done on the optical properties of individual carbon nanotubes. Recently, photoexcited band-gap fluorescence was observed in bulk carbon nanotube samples in which the tubes were incorporated inside micelles (12). In this paper, we show that polarized optical emission can be observed from a single s-SWNT or a small bundle of s-SWNTs dispersed from solution when electrons ( $e^-$ ) and holes ( $h^+$ ) are electrically injected simultaneously.

Carbon nanotube optical sources can be distinguished from semiconductor nanowire sources because in the undoped carbon nanotube optical device, there is no depletion region analogous to that in a conventional p-n junction. Rather, the carbon nanotube source relies on the presence of narrow metal-nanotube Schottky barriers (13, 14) that are present at each junction and allow both  $e^-$  and  $h^+$  injection (15, 16). The recombination radiation is generated in a dopant-free channel and no built-in field is present.

The s-SWNT device we used (Fig. 1A) was a three-terminal FET identical to the ambipolar devices described earlier (15). Fabrication started by randomly dispersing carbon nanotubes  $\sim 1.4$  nm in diameter from solution onto a  $p^+$  silicon substrate with a 150-nm silicon dioxide layer (17, 18). Source and drain contacts were fabricated by means of lithography and lift-off techniques. A 50-nm-thick titanium evaporated film was used to make the source and drain contacts, and the devices were then annealed in argon at a temperature of 850°C. This process has been shown to lead to abrupt junctions with titanium carbide contacts (15). The devices were then capped with a 10-nm silicon dioxide layer deposited at room temperature and densified by first annealing at 400°C for 30 min in forming gas and subsequently annealing at 700°C for 2 min in argon. The electrical characteristics of a typical resulting ambipo-

IBM Research Division, IBM Thomas J. Watson Research Center, Yorktown Heights, NY 10598–0218, USA.

\*Present address: Materials Science Department, Brookhaven National Laboratory, Upton, NY 11973, USA.

## REPORTS

lar FET (Fig. 1B) show that with the source at ground potential and a small drain potential, the device behaves as an n-type conductor by drawing electrons into the channel when the gate potential is positive, and as a p-type material by drawing holes into the channel when the gate potential is negative.

We characterized the optical emission properties of these devices with an infrared (IR) camera (an IR Laboratories  $256 \times 256$  HgCdTe IR camera) mounted on the probe station used to measure their electrical properties. This camera can detect light with wavelengths longer than about 800 nm. However, this camera has a built-in filter that begins to block light at wavelengths longer than 1500 nm. IR images with this camera are typically obtained by integrating the emission for 190 s.

Temperature-dependent electrical transport data, in conjunction with modeling, have shown that the application of a gate field in the s-SWNT device, as in Fig. 1A, results in a Schottky barrier width that allows thermally assisted  $e^-$  or  $h^+$  tunneling through the barrier, depending on the sign of the gate field (15, 16, 19). Simultaneous  $e^-$  and  $h^+$  injection was achieved by biasing the device with the value of the gate potential between those of the source and drain potentials. This biasing scheme results in opposite signs for the gate-induced fields at the source and drain electrodes. For example, consider the case where the source is grounded, the gate is at a potential of +5 V, and the drain is at +10 V. The difference of the potentials of the source and drain with respect to that of the gate is the same (5 V), but the sign of the gate field is opposite at each contact, with the field at the source drawing electrons into the channel while the field at the drain draws holes into the channel (20). A region is created near the source that behaves as an n-type material, and a region is created near the drain behaving as a p-type material, with a higher potential applied to the p-type region. In a simple model, the device can be thought of as a sort of a forward-biased p-n junction. Figure 1C shows a family of curves where the drain current is plotted versus drain voltage ( $V_d$ ) for different values of the gate voltage ( $V_g$ ). For a given  $V_g$  that is below the threshold voltage of the nanotube FET, there is only a small current flowing until  $V_d$  exceeds  $V_g$ . Beyond this point, the current grows nearly exponentially.

A calculated band diagram for this system based on the Schottky barrier transistor model of (16) is shown in Fig. 1D. This model has been shown to reproduce the experimental observations on ambipolar FETs (15). The key features of this band diagram are the Schottky barriers at each metal-nanotube junction. We expect the sum of the barrier heights for  $e^-$  and  $h^+$  to equal the band gap, as is shown in Fig. 1D. However, because of the opposite gate field at each tube end, the tunneling barrier width for

$e^-$  is small at the source, whereas it is small for  $h^+$  at the drain. Thermally assisted tunneling then allows for the efficient injection of both  $e^-$  and  $h^+$  simultaneously at room temperature. Such a band diagram is consistent with the data of Fig. 1C.

Under conditions of simultaneous  $e^-$  and  $h^+$  injection, we observed IR emission from carbon nanotube FET devices. Many different devices were studied, and light emission was observed from every ambipolar SWNT FET tested (>10) and never from unipolar

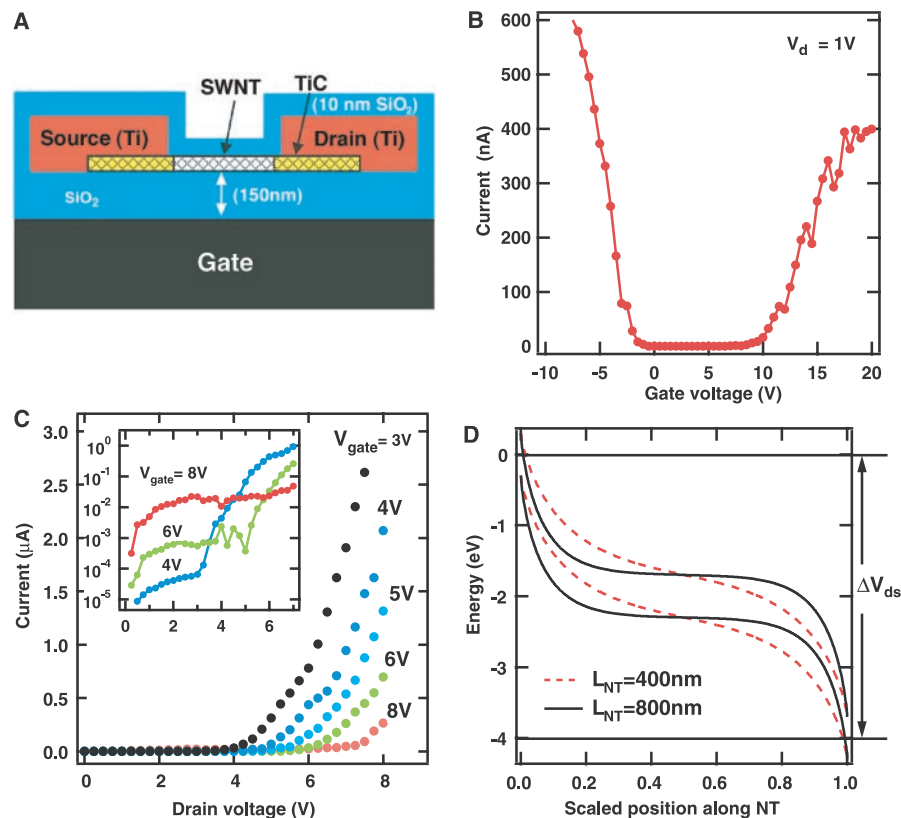
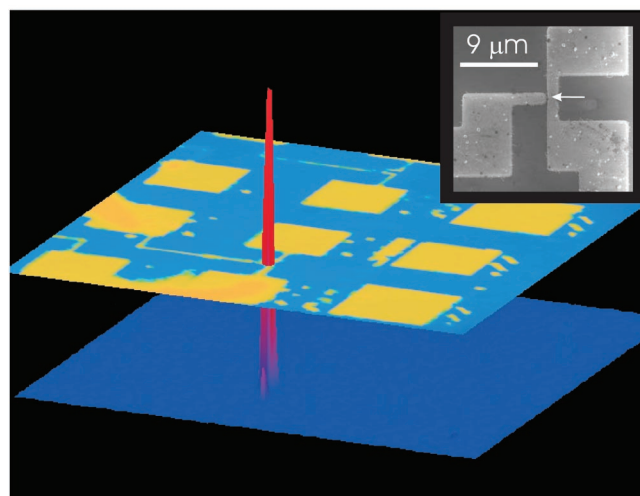


**Fig. 1.** (A) Schematic diagram of the ambipolar s-SWNT device structure. (B) Electrical characterization of a typical ambipolar device. A plot of the drain current versus  $V_g$  for a grounded source and a small drain potential of 1 V is shown. The data indicate ambipolar behavior. (C) Plot of the drain current versus  $V_d$  for a grounded source and a gate potential of 5 V for the device used in the optical measurements. The inset shows the data on a logarithmic scale. (D) Calculated band structure for carbon nanotube FET devices with  $V_d = 4$  V and  $V_g$  halfway between the source and drain voltages. The bands were calculated using channels 800 nm (black) and 400 nm (red) long and a 150-nm silicon dioxide gate insulator layer.

**Fig. 2.** Optical emission from an ambipolar carbon nanotube FET detected with an IR camera. The upper plane is a color-coded IR image of the carbon nanotube FET. The contact pads and thin wires leading to the carbon nanotube channel are shown in yellow. The lower plane is the surface plot of the IR emission image taken under conditions of simultaneous  $e^-$  and  $h^+$  injection into the carbon nanotube. The emission was localized at the position of the carbon nanotube. (Inset) SEM showing the device structure in the region of the nanotube emitter.



nanotube devices ( $>12$ ). As an example, the upper plane in Fig. 2 shows a color-coded IR image of an entire chip. This picture was obtained using the IR camera with the sample under IR illumination. The blue area shows the silicon dioxide, whereas the yellow area shows the metallization providing contacts to the carbon nanotube. Large pads used for contact in the probe station are shown in yellow (the pads are  $\sim 70 \mu\text{m}$  square). The narrower yellow lines show the metal wires that form a small gap ( $\sim 300 \text{ nm}$ ); the separation between source and drain that is bridged by the nanotube channel [see a closeup scanning electron microscopy (SEM) image in the inset of Fig. 2]. A darker orange-yellow region shows the probes contacting the pads to measure the electrical properties of the device. The nanotube itself cannot be seen with the IR imaging because of the limited spatial resolution of  $1 \mu\text{m}$ . However, SEM images and electrical measurements confirm that the nanotube bridges the gap at the ends of the metallization. Finally, the lower plane is a color-coded surface plot of the intensity of the IR emission from a biased device. This image was obtained by eliminating all background light and obtaining an IR camera image while current was flowing through the device. When both  $e^-$  and  $h^+$  were injected (as in Fig. 1C), then IR emission was observed. Data were obtained using a 190-s integration time while a parameter analyzer repeatedly swept  $V_d$  between 0 and 10 V in about 3 s, while keeping the source grounded and  $V_g$  fixed at +5 V. We used this sweeping technique in order to avoid threshold shifts that may occur because of mobile charges present on the gate oxide.

Because the approximately 1.4-nm-diameter carbon nanotubes have a band gap of  $\sim 750 \text{ meV}$  (21, 22), which corresponds to a wavelength of approximately 1650 nm, the

camera observes emission that is on the high-energy side of the peak of the band-gap emission. However, the detected intensity of the emission is high and therefore indicates that the recombination peak is significantly broadened, probably because of a shorter lifetime associated with the direct interactions with the metal contacts and the presence of electric field gradients. The emission is highly localized in the IR camera image in Fig. 2 at the position of the nanotube; the emission intersects the upper panel at the location where the nanotube bridges the source and drain electrodes. When either an electron or hole unipolar current flowed through the device, for example when a small voltage was applied to the drain and a large voltage to the gate (as in Fig. 1B), no IR emission was observed, even at higher currents (and higher power), demonstrating that thermal heating is not the source of the observed IR light.

Experiments under different electrical biasing conditions provide further evidence that the nature of the IR emission is recombination radiation in the nanotube resulting from the simultaneous injection of  $e^-$  and  $h^+$ . Figure 3A shows the emission intensity determined in a series of experiments where the gate voltage was fixed at a value  $V_g$  while the drain voltage was swept repeatedly from 0 volts to  $V_d$ , corresponding to the electrical transport data shown in Fig. 1C. The red data points are for a  $V_d = 8 \text{ V}$ , whereas the blue points give the intensity for  $V_d = 4 \text{ V}$ , as a function of  $V_g$  (a background level was subtracted out to help the comparison with the theoretical curves). Starting at  $V_g = 8 \text{ V}$ , no emission was observed. This result is consistent with our Schottky barrier model for the behavior of this system, because  $V_d$  did not exceed  $V_g$  and thus there was a wide barrier inhibiting  $h^+$  injection. As  $V_g$  was decreased,

the IR emission intensity grew because of the increasing  $h^+$  current and reached a maximum at about  $V_g = V_d/2$ . When  $V_g$  was lowered further, the total current in the system continued to increase (see Fig. 1C), but the IR emission intensity decreased. For comparison, the total electrical power in the channel is also plotted in Fig. 3B, showing that as  $V_g$  was lowered, the power continued to increase. The IR emission peaked near  $V_g = V_d/2$ , where the injected  $e^-$  and  $h^+$  currents were about equal because the fields acting on the source and drain Schottky barriers had about the same magnitude (but opposite direction). At lower  $V_g$ , the current became more unipolar and the emission decreased. A calculation based on the Schottky barrier model (16) of the variation of the IR emission with  $V_g$  is shown by the solid lines in Fig. 3A. This model assumes that the emission intensity is determined by the current of the minority carrier. The calculated emission intensity is scaled to the observed intensity at  $V_d = 4 \text{ V}$ . The model predicts a maximum emission at  $V_g = V_d/2$ , as is observed experimentally, with increasing emission at higher  $V_d$ . In addition, the model fits very well the relative intensity of the emission peaks, but

**Fig. 3.** (A) IR emission intensity during repeated sweeps of the drain potential from 0 V to  $V_d$  as a function of gate potential  $V_g$ . The red data (triangles) are for  $V_d = 8 \text{ V}$ , and the blue data (circles) are for  $V_d = 4 \text{ V}$ . The blue data are multiplied by 5. For a given  $V_d$ , the IR emission shows a maximum when  $V_g = V_d/2$ . The full curves give the computed emission at constant  $V_d$ , assuming that recombination is limited by the lesser of the  $h^+$  or  $e^-$  currents. The theoretical current is normalized to the maximum emission detected at  $V_d = 8 \text{ V}$ . The black dotted line indicates the intensity of a background subtracted from all the IR emission data. The dashed line is a curve to guide the eye. (B) The total electrical power per scan of the device during the sweeps corresponding to the red data.

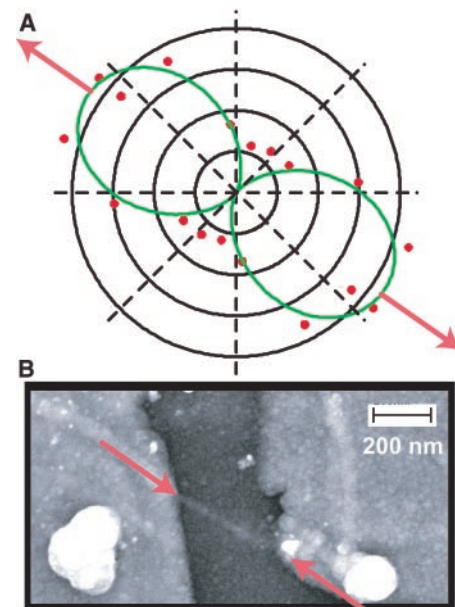
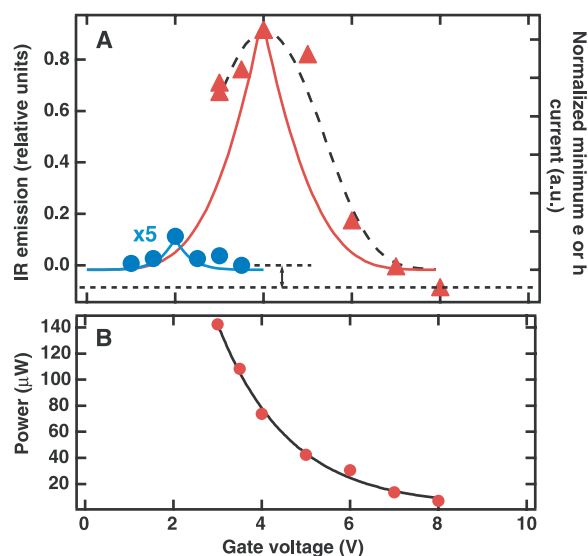


**Fig. 4.** Polarization dependence of the optical emission intensity from an ambipolar carbon nanotube FET. (A) The data (red dots) are shown in the form of a polar plot of the intensity versus analyzer angle  $\theta$  (accuracy is about  $10^\circ$ ). The green curves are a fit of the data to a  $\cos^2\theta$  dependence. (B) An SEM image of the emitting device showing the region near the nanotube channel. The whole device is covered by 10 nm of  $\text{SiO}_2$ . The red arrows in (A) and in (B) mark the polarization direction and the orientation of the nanotube, respectively. Unique polarization analysis data were only attained for a  $180^\circ$  sweep of the analysis angle; however, the data are plotted in a standard  $360^\circ$  plot for ease of comparison.

## REPORTS

this agreement may be fortuitous. An alternative model, based on the product of  $e^-$  and  $h^+$  currents, gives a poor description of the relative intensities but a good description of the peak width for  $V_d = 8$  V. The key point is that the maximum in emission at  $V_g = V_d/2$  is a clear signature of emission caused by carrier recombination in an ambipolar Schottky barrier transistor.

The optical emission from the nanotube devices was further characterized by measuring its polarization. For this purpose, an IR polarizer was inserted between the sample and the IR camera. Figure 4A presents an example of a polar plot showing the intensity of the IR emission (red dots) as a function of the polarization angle from a device operating with  $V_g = 4$  V and  $V_d = 8$  V. The carbon nanotube is expected to be a linearly polarized dipole radiation source. When the radiating dipole makes an angle  $\theta$  with respect to the polarizer analysis axis, the component of the emitted field along the polarizer axis is proportional to  $\cos\theta$ . The transmitted intensity therefore is proportional to  $\cos^2\theta$ . The green lines in Fig. 4 show this ideal  $\cos^2\theta$  dependence. The measured data are in reasonable agreement with the expected behavior of a linearly polarized source. Also shown in Fig. 4B is an SEM image of the device covered with  $\text{SiO}_2$  oxide, which shows that the peak in the polarized emission occurs when the polarizer is aligned parallel to the carbon nanotube axis.

Because the band gap in carbon nanotubes is inversely proportional to the tube diameter, one should be able to control the wavelength of the optical emission by using tubes of different diameters. In addition, an aggressive scaling of the gate oxide thickness and the use of an insulator with a high dielectric constant are expected to improve the injection efficiency and emission yield, and reduce the operation voltage. Thus, carbon nanotubes offer great promise as a compact, easy-to-integrate nanoscale source of photons for future photonic and optoelectronic devices.

### References and Notes

- J. Wang, M. S. Gudiksen, X. Duan, Y. Cui, C. M. Lieber, *Science* **293**, 1455 (2001).
- X. Duan, Y. Huang, Y. Cui, J. Wong, C. M. Lieber, *Nature* **409**, 66 (2001).
- M. S. Gudiksen, L. J. Lauhon, J. Wong, D. C. Smith, C. M. Lieber, *Nature* **415**, 617 (2002).
- S. Tans, A. Verschuere, C. Dekker, *Nature* **393**, 49 (1998).
- R. Martel, T. Schmidt, H. R. Shea, T. Hertel, Ph. Avouris, *Appl. Phys. Lett.* **73**, 2447 (1998).
- H. T. Soh et al., *Appl. Phys. Lett.* **75**, 627 (1999).
- V. Derycke, R. Martel, J. Appenzeller, Ph. Avouris, *Nano Lett.* **1**, 453 (2001).
- X. Liu, C. Lee, C. Zhou, J. Han, *Appl. Phys. Lett.* **79**, 3329 (2001).
- A. Bachtold, P. Hadley, T. Nakanishi, C. Dekker, *Science* **294**, 1317 (2001).
- A. M. Rao et al., *Science* **275**, 187 (1997).
- R. Saito, H. Kataura, in *Carbon Nanotubes: Synthesis, Structure, Properties, and Applications*, M. S. Dresselhaus, G. Dresselhaus, Ph. Avouris, Eds. (Springer-Verlag, Berlin, 2001), pp. 213–247.
- M. J. O'Connell et al., *Science* **297**, 593 (2002).
- M. S. Fuhrer et al., *Science* **288**, 494 (2000).
- M. Freitag, M. Radosavljevic, Y. X. Zhou, A. T. Johnson, W. F. Smith, *Appl. Phys. Lett.* **79**, 3326 (2001).
- R. Martel et al., *Phys. Rev. Lett.* **87**, 256805 (2001).
- S. Heinze et al., *Phys. Rev. Lett.* **89**, 106801 (2002).
- The SWNTs were prepared by laser ablation as described in (18). They were used without further treatment and were dispersed in dichloroethane by a short exposure to ultrasound.
- A. Thess et al., *Science* **273**, 483 (1996).
- J. Appenzeller et al., *Phys. Rev. Lett.* **89**, 126801 (2002).
- A. Dodabalapur, H. E. Katz, L. Torsi, R. C. Haddon, *Appl. Phys. Lett.* **68**, 1108 (1996).
- S. M. Bachilo et al., *Science* **298**, 2361 (2002).
- A. Hagen, T. Hertel, *Nano Lett.* **3**, 383 (2003).
- We thank R. Smalley and A. Rinzler for supplying the SWNT sample, J. Appenzeller for helpful discussions, K. K. Chan for device processing, and the referee for valuable suggestions.

9 December 2002; accepted 26 March 2003

# The Potential for Earthquake Early Warning in Southern California

Richard M. Allen<sup>1\*</sup> and Hiroo Kanamori<sup>2</sup>

Earthquake mitigation efforts in the United States currently use long-term probabilistic hazard assessments and rapid post-earthquake notification to reduce the potential damage of earthquakes. Here we present the seismological design for and demonstrate the feasibility of a short-term hazard warning system. Using data from past earthquakes, we show that our Earthquake Alarm System (Elarms) could, with current TriNet instrumentation, issue a warning a few to tens of seconds ahead of damaging ground motion. The system uses the frequency content of the P-wave arrival to determine earthquake magnitude, an approach that allows magnitude determination before any damaging ground motion occurs.

Current efforts to mitigate seismic hazard in the United States include long-term (50-year) hazard assessment and rapid post-event notification. Long-term hazard mitigation is facilitated by probabilistic ground-shaking maps (1), which estimate the probability of ground motion exceeding some threshold during the next 50 years. Such maps are used in the development of building codes intended to prevent the collapse of buildings during an earthquake. Rapid post-event notification in southern California is provided by TriNet (now part of the California Integrated Seismic Network), a network of about 155 station sites with both high dynamic-range broadband and strong-motion instrumentation (2, 3). Rapid notification of earthquake source parameters is issued through a pager system called CUBE (4) and over the Internet, within minutes of substantial earthquakes. Peak ground motion observations are also used to generate a map of ground motion distribution ("ShakeMap") within 3 to 5 min of an earthquake (5).

Earthquake early warning systems (EWSs) provide a few seconds to tens of seconds of warning of oncoming ground motion, allowing for short-term mitigation. EWSs that estimate

the severity of ground shaking and the time till that shaking will commence are in operation in Japan, Mexico, and Taiwan. The most basic system, offering no warning time, issues an alarm when ground shaking at the same location exceeds some threshold. When the earthquake source region is some distance from a populated area or city, seismometers can be deployed between the source and the city to detect any earthquake and transmit a warning electronically, ahead of the more slowly moving ground motion. Mexico City is protected by such a front-detection EWS: Seismometers along the coast detect earthquakes in the Guerrero Gap ~300 km southwest of the city and an alarm is issued, providing ~70 s of warning time (6, 7). The Central Weather Bureau of Taiwan also uses a front-detection EWS, which requires an average of 22 s to determine earthquake magnitude and location and thus provides warning for areas greater than ~75 km from the epicenter (8, 9).

All these EWSs use observations of peak ground motion to estimate the magnitude of an earthquake, which is the most commonly applied and most accurate method of local magnitude determination. However, this approach does not provide the most rapid magnitude estimate. The first seismic arrival from an earthquake is the P wave, which is usually relatively low-amplitude and causes little damage (Fig. 1). It is followed by the S wave, which usually has a larger amplitude and includes the peak ground motion (Fig. 1),

<sup>1</sup>Department of Geology and Geophysics, University of Wisconsin, Madison, WI 53706, USA. <sup>2</sup>Seismological Laboratory, California Institute of Technology, Pasadena, CA 91125, USA.

\*To whom correspondence should be addressed. E-mail: rallen@geology.wisc.edu